# The effect of titanium dioxide-supported CdSe photocatalysts enhanced for photocatalytic glucose electrooxidation under UV illumination

Aykut Caglar [a], Hilal Kivrak [b,d,**], Nahit Aktas [a,c,*]

[a] Van Yuzuncu Yil University, Faculty of Engineering, Department of Chemical Engineering, VAN, Turkey
[b] Eskisehir Osmangazi University, Faculty of Engineering and Architectural Sciences, Department of Chemical Engineering, ESKİŞEHİR, Turkey
[c] KyrgyzTurk Manas University, Faculty of Engineering, Department of Chemical Engineering, BİSHKEK, Kyrgyzstan
[d] Translational Medicine Research and Clinical Center, Eskisehir Osmangazi University, 26040 Eskisehir, Turkey

## HIGHLIGHTS

- $TiO_2$ is the most common semiconductor used in photocatalytic applications.
- Cd and Se are metals with quantum dot properties.
- Wet-impregnation, the most widely used method in catalyst synthesis.
- Glucose is an organic material containing high energy in its structure.

## ARTICLE INFO

## ABSTRACT

The wetness impregnation method was used to synthesize 0.1% $CdSe/TiO_2$ photocatalysts with different atomic molar ratios (90—10, 70—30, 50—50, and 30—70). These catalysts were characterized by XRD, SEM-EDX and mapping, TEM-EDS, UV–VIS spectroscopy, fluorescence spectroscopy, XPS, TPR, TPO, and TPD analyses. Cyclic voltammetry (CV), chronoamperometry (CA), and electrochemical impedance spectroscopy (EIS) analyses were performed to examine the photocatalytic activity for photocatalytic fuel cells (PFCs) in glucose solution in the dark and under UV illumination. The characterization analyses revealed that anatase $TiO_2$ formed the catalyst and electronic structure and surface properties changed when doped with metal. The photocatalytic glucose electrooxidation (PGE) results demonstrate that the 0.1% $CdSe(50-50)/TiO_2$ catalyst has higher photocatalytic activity, stability, and resistance than other catalysts both in the dark (2.71 mA cm$^{-2}$) and under UV illumination (7.20 mA cm$^{-2}$). These results offer a promising new type of photocatalyst for PFC applications.

\* *Corresponding author.* Van Yuzuncu Yil University, Faculty of Engineering, Department of Chemical Engineering, VAN, Turkey.
\*\* *Corresponding author.*
E-mail addresses: hilaldemir.kivrak@ogu.edu.tr, hilalkivrak@gmail.com (H. Kivrak), nahit.aktas@manas.edu.kg, naktas@yyu.edu.tr (N. Aktas).

## Introduction

Nowadays, with the increasing energy demands and the reduction in conventional energy sources such as wood, coal, oil and natural gas, meeting energy needs has become a major problem. Until now, energy needs have been met by conventional energy sources [1]. However, the depletion of fossil fuels is accelerating as the population increases and industry grows. Furthermore, these energy sources, which contribute 80% of the world's primary energy, negatively affect the environment with climate change caused by harmful gases such as carbon dioxide, sulfur oxide, and nitric oxide [2—4]. Therefore, researchers have turned to alternative energy sources. Alternative energy sources were examined in many fields in the literature such as water splitting [5], fuel cells [6], hydrogen storage [7], supercapacitors [8], solar energy [9], and lithium-ion batteries [10]. As clean energy sources among these alternative energy sources, fuel cells have attracted the attention of the scientific world to meet the world's energy demand as one of the most important energy sources in the future. Fuel cells are promising as a sustainable and efficient energy source for a clean future that converts chemical energy directly into electrical energy [11—14]. Fuel cells can be grouped into two systems. These are high and low temperature fuel cells. High temperature fuel cells (over 873 K) are molten carbonate fuel cells and solid oxide fuel cells, while low temperature fuel cells (below 473 K) are systems such as alkaline fuel cells, direct alcohol fuel cells, phosphoric acid fuel cells, and polymer electrode fuel cells [15]. Photocatalytic fuel cells (PFC), which include semiconductor photoanode, cathode, and electrolyte such as methanol [16], ethanol [17], and glucose ($C_6H_{12}O_6$) [18], are promising devices that can handle the energy crisis and environmental pollution by utilizing sunlight as energy input. Glucose is used as fuel in alkaline fuel cells, which is a low temperature fuel cell [19]. Gao et al. [20] reported direct glucose fuel cell analysis of Ni—Co composites supported by activated carbon in alkaline medium. They emphasized that the anode composites they obtained had high performance for direct glucose fuel cell in alkaline environment. Glucose is a high energy density (4.43 kWh/kg), non-toxic, flammable and non-volatile, potential hydrogen carrier and is the most abundant simple sugar in nature [21—25]. A glucose molecule can produce 24 electrons and yield −2870 kJ/mol of energy via complete oxidation to $CO_2$. It is worth noting that it consists mostly of gluconic acid and was used a two-electron generating system in all studies to date [26].

Metal, metal oxide nanoparticles, enzymes, and semiconductor materials have been widely investigated for the catalytic oxidation of glucose, which is utilized as a renewable energy source to satisfy energy demands [27]. Photocatalysis changes the rate of a chemical reaction when a semiconductor material is exposed to light. Semiconductor materials are photocatalysts that absorb light and act as catalysts for chemical reactions [28]. Materials such as titanium dioxide ($TiO_2$), zinc oxide (ZnO), and tin dioxide ($SnO_2$) are semiconductor materials used as photocatalysts in the literature [29]. $TiO_2$ (3.2 eV wide band gap [30]), which was first

discovered by Fujishima and Honda in 1972 with its water separation feature, was used as photoanode [31].

$TiO_2$ has the disadvantage that it adsorbs less than 5% of the solar source of UV light and causes rapid recombination of photogenerated electron-hole pairs, leading to low quantum yield and activity for PFCs. Researchers have studied $TiO_2$-based metals [32], metal sulfides [33], metal oxides [34], and carbon-based materials [35] to improve their photocatalytic activity for use in PFCs. Recently, $TiO_2$ was used as a semiconductor material for photocatalytic and photovoltaic applications. For these applications, semiconductor nanocrystal quantum dots were used with different metals to sensitize $TiO_2$. These structures have advantages such as thermal stability, not easily photodegrading, and having large absorption cross-sections. Metals such as Cd and Se comprise a type II band alignment with $TiO_2$. CdSe-modified $TiO_2$ can be used to initiate photocatalytic reactions [36,37]. In addition, it is emphasized that catalysts with CdSe structure exhibit stable photocurrent density [38]. Hu et al. [39] investigated the effects of photocatalytic degradation mechanisms of different organic classes and comprehensive characterization of photoelectrochemical properties by optimization of $TiO_2$, $WO_3$ and $Nb_2O_5$ photoanodes with statistical 2 k factorial design for PFCs. They emphasized that the $TiO_2$-based PFC gave the highest photocurrent density as a result of its high intrinsic quantum efficiency compared to the others. In addition, CNT/nano-$TiO_2$/Pt complex electrode (13 mA/cm$^2$) [40], NiO—$TiO_2$—$ZrO_2$/$SO_4^{2-}$ (5.19 mA/cm$^2$) [41], Cu/$Cu_2O$/TNT (6.40 mA/cm$^2$) [42], Ni(OH)$_2$—24.2%/TNT (23.43 mA/cm$^2$) [43], and C-TNT (9.10 mA/cm$^2$) (UV illumination) [44] materials were studied for glucose electrooxidation in literature. Photocatalytic performances of semiconductor materials such as $TiO_2$ with different metals were investigated in many areas such as decomposition, hydrogen production, and $CO_2$ reduction [45,46].

Although there are many photocatalytic studies, photocatalytic electrooxidation studies of photoanode catalysts for fuel cells are not available in the literature, except for a few studies. In the present study, CdSe/$TiO_2$ photocatalysts were synthesized at different atomic molar ratios (90:10, 70:30, 50:50, 30:70) by utilizing the wetness impregnation method. The reduction process was realized in a furnace under argon gas at 400 °C. The structure of catalysts was characterized by using XRD, SEM-EDX and mapping, TEM, XPS, UV-VIS spectroscopy, fluorescence spectroscopy, TPR, TPO, and TPD analyses. Cyclic voltammetry (CV), chronoamperometry (CA), and electrochemical impedance spectroscopy (EIS) analyses were performed to examine the catalytic activity of PGE in the dark and under UV illumination.

## Experimental

### Synthesis of CdS/$TiO_2$ catalysts

All chemicals were bought from Sigma-Aldrich and Acros Organics. CdSe/$TiO_2$ catalysts were synthesized in different ratios by using the wetness impregnation method. The Cd loading was adjusted to 0.1% by weight. Firstly, the appropriate amounts of Cd ($CdCl_2$ x $H_2O$, 99.995%) and Se ($Na_2SeO_3$,
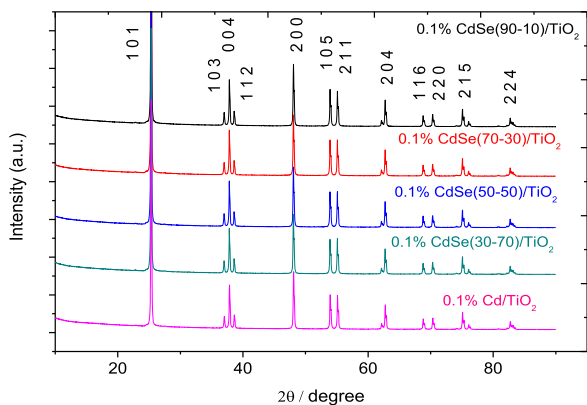
**Fig. 1 – XRD patterns of 0.1% CdSe/TiO₂ catalysts.**

44–46%) precursors were distributed under sonication with DI water in a beaker for 0.1% CdSe/TiO₂ catalysts. After the metal precursors were homogeneously dispersed in DI water, TiO₂ (99%) was added and mixed for 30–60 min with the help of a glass rod. It was then left to dry at 85 °C overnight. Finally, the reduction process of the obtained catalysts was performed under argon gas for 2 h at a heating rate of 10 °C/min up to 400 °C in a furnace. Cooling was carried out with the help of a fan. 0.1% CdSe/TiO₂ catalysts were synthesized under the same synthesis conditions with (90–10), (70–30), (50-50), and (30–70) metal ratios.

*Characterization of CdSe/TiO₂ catalysts*

X-ray Diffraction (XRD) patterns were obtained to examine crystal structures with an Empyrean (PANanalytical) diffractometer using Cu-Kα ($\lambda = 1.5406$ Å) radiation source. The surface morphologies of catalysts were characterized utilizing SEM-EDX and mapping (ZEISS Sigma 300) analysis. TEM

analysis was obtained using the Hitachi HighTech HT7700 device at 120 kV accelerating voltage and a maximum resolution of 0.204 nm. UV–VIS spectra were recorded with the Shimadzu UV-3600 Plus device. The fluorescence spectrum of catalysts was measured with a PerkinElmer FL6500 fluorescence spectrophotometer. The elemental composition and oxidation state of the 0.1% CdSe(50-50)/TiO₂ catalyst was examined using XPS analysis (Specs-Flex) with a CCD detector (Kα (Al): 1486.7 eV). Micromeritics Chemisorb 2750 equipment was used to examine H₂-TPR, O₂-TPO, and NH₃-TPD analyses with an automated system linked to ChemiSoft TPx software.

*Photo-electrochemical measurements*

CV, CA, and EIS electrochemical analyses of the catalysts were performed using CHI 660 and 601 E potentiostat devices to examine activity, stability, and resistance, respectively. All analyses were performed in a three-electrode system with a reference electrode (Ag/AgCl), working electrode (Titanium metal, 0.4 mm thickness), and counter electrode (Pt wire) in 1 M KOH and 1 M KOH + 0.5 M glucose solution. The catalyst slurry was obtained by mixing CdSe/TiO₂ catalysts and Nafion and it was transferred using titanium metal with 0.5 cm² area. CV, CA, and EIS analyses were used to investigate catalytic activities of PGE in the dark and under UV illumination. The UV lamp used for illumination had a power of 366 nm (long wavelength) and 6 W in a cabinet connected to the UVP device.

## Results and discussion

*Physical characterization*

X-ray diffraction (XRD) is utilized to define the structure of crystalline materials. Fig. 1 indicates the XRD patterns of Cd/TiO₂ and CdSe/TiO₂ catalysts. The main peaks for anatase TiO₂

**Table 1 – Diffraction peaks of XRD patterns at 2θ for TiO₂, Cd/TiO₂, and CdSe/TiO₂ catalysts.**

Observed (degree)

| (hkl) planes | TiO₂ | Cd/TiO₂ | CdSe(90–10)/TiO₂ | CdSe(70–30)/TiO₂ | CdSe(50-50)/TiO₂ | CdSe(30–70)/TiO₂ |
|---|---|---|---|---|---|---|
| (101) | 25.32 | 25.32 | 25.32 | 25.32 | 25.32 | 25.32 |
| (103) | 36.89 | 36.96 | 37.04 | 36.93 | 36.90 | 36.92 |
| (004) | 37.95 | 37.90 | 37.88 | 37.87 | 37.85 | 37.89 |
| (112) | 38.72 | 38.69 | 38.58 | 38.64 | 38.59 | 38.58 |
| (200) | 48.23 | 48.13 | 48.11 | 48.12 | 48.07 | 48.02 |
| (105) | 53.91 | 53.96 | 54.00 | 53.88 | 53.92 | 53.94 |
| (211) | 55.20 | 55.06 | 55.12 | 55.12 | 55.15 | 55.09 |
| (204) | 62.85 | 62.76 | 62.67 | 62.72 | 62.76 | 62.75 |
| (116) | 68.90 | 68.82 | 68.79 | 68.79 | 68.75 | 68.81 |
| (220) | 70.31 | 70.34 | 70.30 | 70.34 | 70.25 | 70.31 |
| (215) | 75.12 | 75.10 | 75.10 | 75.07 | 75.15 | 75.06 |
| (224) | 82.78 | 82.77 | 82.70 | 82.71 | 82.65 | 82.72 |

**Table 2 – Structural parameters of TiO₂, Cd/TiO₂, and CdSe/TiO₂ catalysts.**

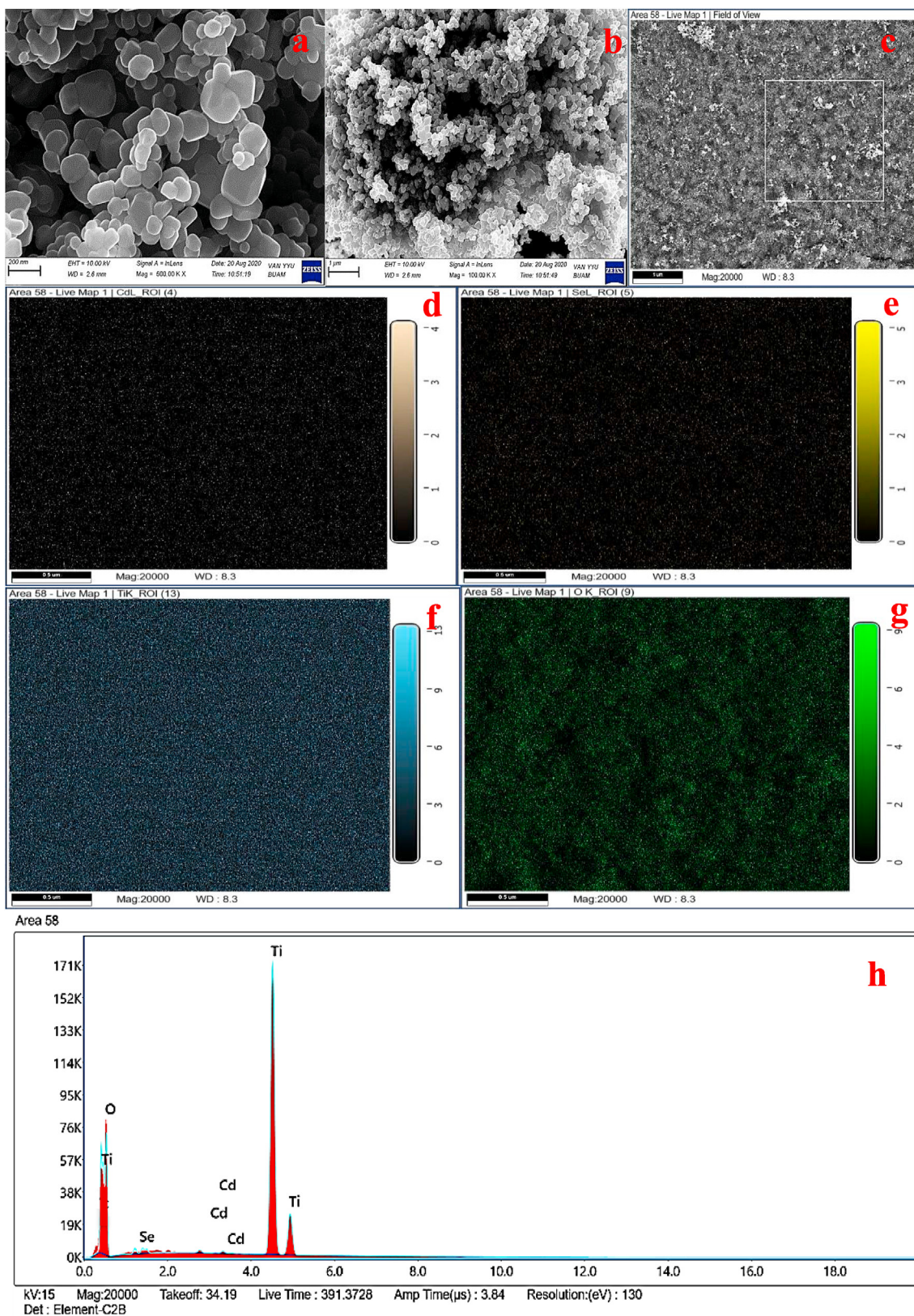| Parameters | TiO₂ | Cd/TiO₂ | CdSe(90–10)/TiO₂ | CdSe(70–30)/TiO₂ | CdSe(50-50)/TiO₂ | CdSe(30–70)/TiO₂ |
|---|---|---|---|---|---|---|
| crystallite size (D, nm) | 50.10 | 51.69 | 52.38 | 51.55 | 50.03 | 51.46 |
| dislocation density ($\delta \ast 10^{-3}$ (nm$^{-2}$)) | 0.39 | 0.37 | 0.36 | 0.38 | 0.40 | 0.38 |
| microstrain ($\varepsilon$) ($10^{-3}$) | 3.29 | 3.19 | 3.15 | 3.20 | 3.30 | 3.21 |

Fig. 2 – SEM-EDX and mapping images (Cd (d), Se (e), Ti (f), O (g)) of 0.1% CdSe(50-50)/TiO$_2$ (a-c, h) catalyst.

**Table 3 – Elemental weight composition of 0.1% CdSe/TiO$_2$ catalysts.**

| Elements (%) | Samples | | | |
|---|---|---|---|---|
| | 0.1% CdSe(90–10)/TiO$_2$ | 0.1% CdSe(70–30)/TiO$_2$ | 0.1% CdSe(50-50)/TiO$_2$ | 0.1% CdSe(30–70)/TiO$_2$ |
| Cd | 0.09 | 0.13 | 0.09 | 0.31 |
| Se | 0.47 | 0.05 | 0.51 | 0.23 |
| Ti | 67.17 | 71.00 | 68.24 | 80.42 |
| O | 32.27 | 28.82 | 31.16 | 19.04 |
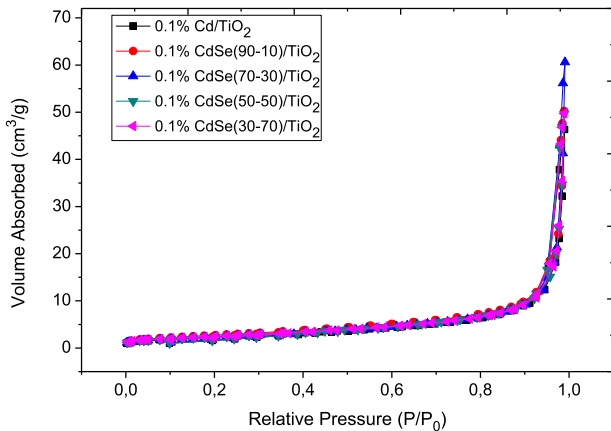


**Fig. 3 – N$_2$ adsorption-desorption isotherms of Cd/TiO$_2$ and CdSe/TiO$_2$ catalysts.**

in both Cd/TiO$_2$ and CdSe/TiO$_2$ catalysts can be clearly determined in the XRD pattern (JCPDS: 21–1272) [47]. All the diffraction peaks in the XRD models appeared to describe the TiO$_2$ anatase phase well. However, characteristic peaks of CdSe may not have formed due to the low metal content in the CdSe/TiO$_2$ catalysts and the crystal plane (111) diffraction peak of CdSe being almost in the same position as the (101) peak of anatase TiO$_2$ [48,49]. Huang et al. [50] emphasized the crystal structural properties of CdS-doped TiO$_2$ by XRD analysis and reported that no peak formed due to the low amount of CdS and good dispersion into TiO$_2$. Table 1 shows the diffraction peaks at 2θ of all catalysts. The difference in diffraction peak positions can be due to metal doping of TiO$_2$ (see Table 1).

The crystallite size (D), dislocation density (δ), and microstrain (ε) of catalysts were appraised through experimental data obtained by XRD analysis (see Table 2). These were calculated with the equations given in the literature [51,52]. It is known that parameters such as crystallite size, microstrain, and dislocation density have an effect on catalytic activity. As

microstrain and dislocation density increase, it inhibits grain growth. This increases catalytic activity by limiting the recombination rate of photo-excited charge carriers in semiconductor materials [51]. In addition, it was emphasized in many studies that decreasing the size of the crystallites increased the catalytic activity [53,54].

SEM-EDX and mapping analyses were performed to examine the surface morphology of the CdSe(50-50)/TiO$_2$ catalyst. Fig. 2a, b illustrates the SEM images (200 nm and 1 μm) of the catalyst. Since the amount of metal used during the synthesis is very low compared to TiO$_2$, TiO$_2$ structures were mostly seen in SEM images. This indicates that the metals did not agglomerate and are well dispersed. Cd, Se, Ti, and O structures were confirmed to form with EDX and mapping analysis. According to the EDX analysis results, the presence of Cd and Se was observed in all CdSe/TiO$_2$ catalysts (Table 3 and Fig. 2h). In Table 3 and Fig. 2h, it can be seen that Cd and Se metals had different ratios in the EDX analysis. Furthermore, the formation of CdSe/TiO$_2$ catalyst was shown by mapping analysis as brown, yellow, turquoise, and green particles formed, which indicate the presence of Cd, Se, Ti, and O, respectively (Fig. 2d–g).

Fig. 3 and Table 4 show the N$_2$ adsorption-desorption isotherms of catalysts. It can be seen in Fig. 3 that the catalysts have a type III adsorption isotherm [55]. The surface area of CdSe/TiO$_2$ catalysts affects catalytic performance. It was found that the specific surface areas of all Cd and CdSe catalysts obtained were in the order of CdSe(50-50)/TiO$_2$ >- CdSe(70–30)/TiO$_2$ > CdSe(30–70)/TiO$_2$ > CdSe(90–10)/ TiO$_2$ > Cd/TiO$_2$. CdSe(50-50)/TiO$_2$ catalyst had the highest surface area and lowest pore and nanoparticle size.

Fig. 4 illustrates the TEM images of the 0.1% CdSe(50-50)/ TiO$_2$ catalyst. In addition, EDX analysis and particle size distribution were performed for the catalyst. As seen in Fig. 4a–g, the particles didn't agglomerate and were generally homogeneously dispersed. TiO$_2$ structures have larger particle size, while CdSe metal particles have evenly distributed and smaller particle size [56]. The particle size histogram of the

**Table 4 – BET surface area, pore-volume, pore size, and nanoparticle size analysis for all catalysts.**

| Sample | BET Surface Area (m$^2$/g) | Pore Volume (cm$^3$/g) | Pore Size (nm) | Nanoparticle Size (nm) |
|---|---|---|---|---|
| 0.1% Cd/TiO$_2$ | 6.63 | 0.0713 | 29.278 | 905.37 |
| 0.1% CdSe(90–10)/TiO$_2$ | 6.85 | 0.0766 | 30.018 | 876.16 |
| 0.1% CdSe(70-30)/TiO$_2$ | 7.00 | 0.0934 | 36.717 | 856.42 |
| 0.1% CdSe(50-50)/TiO$_2$ | 7.50 | 0.0776 | 27.530 | 800.55 |
| 0.1% CdSe(30–70)/TiO$_2$ | 7.07 | 0.0767 | 27.66 | 848.13 |
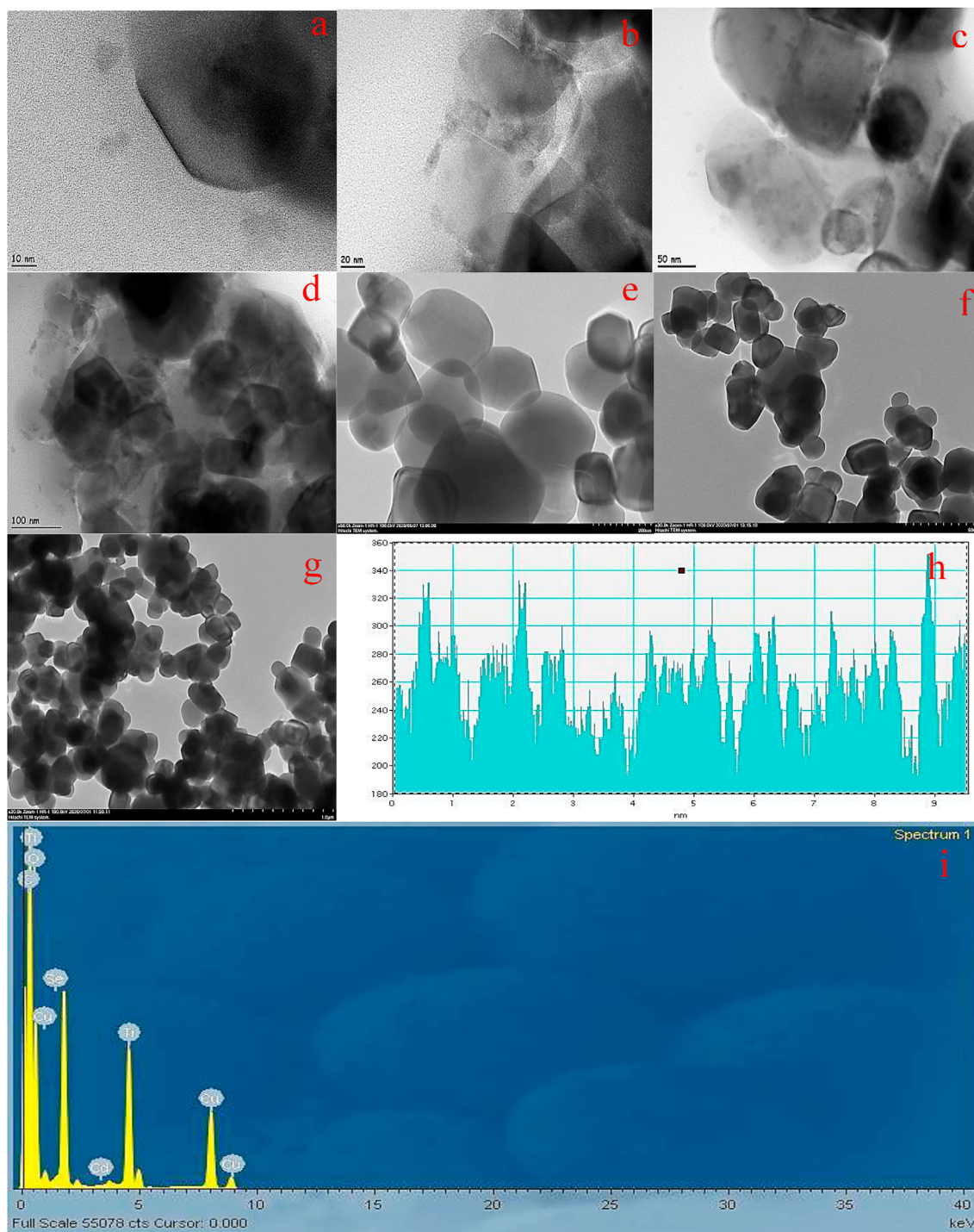
**Fig. 4** — TEM images of 0.1% CdSe(50-50)/TiO$_2$ catalyst (a) 10 nm, (b) 20 nm, (c) 50 nm, (d) 100 nm, (e) 200 nm, (f) 500 nm, (g) 1 μm (h) 10 nm particle size histogram with related particle size distribution, and (i) EDS analysis.
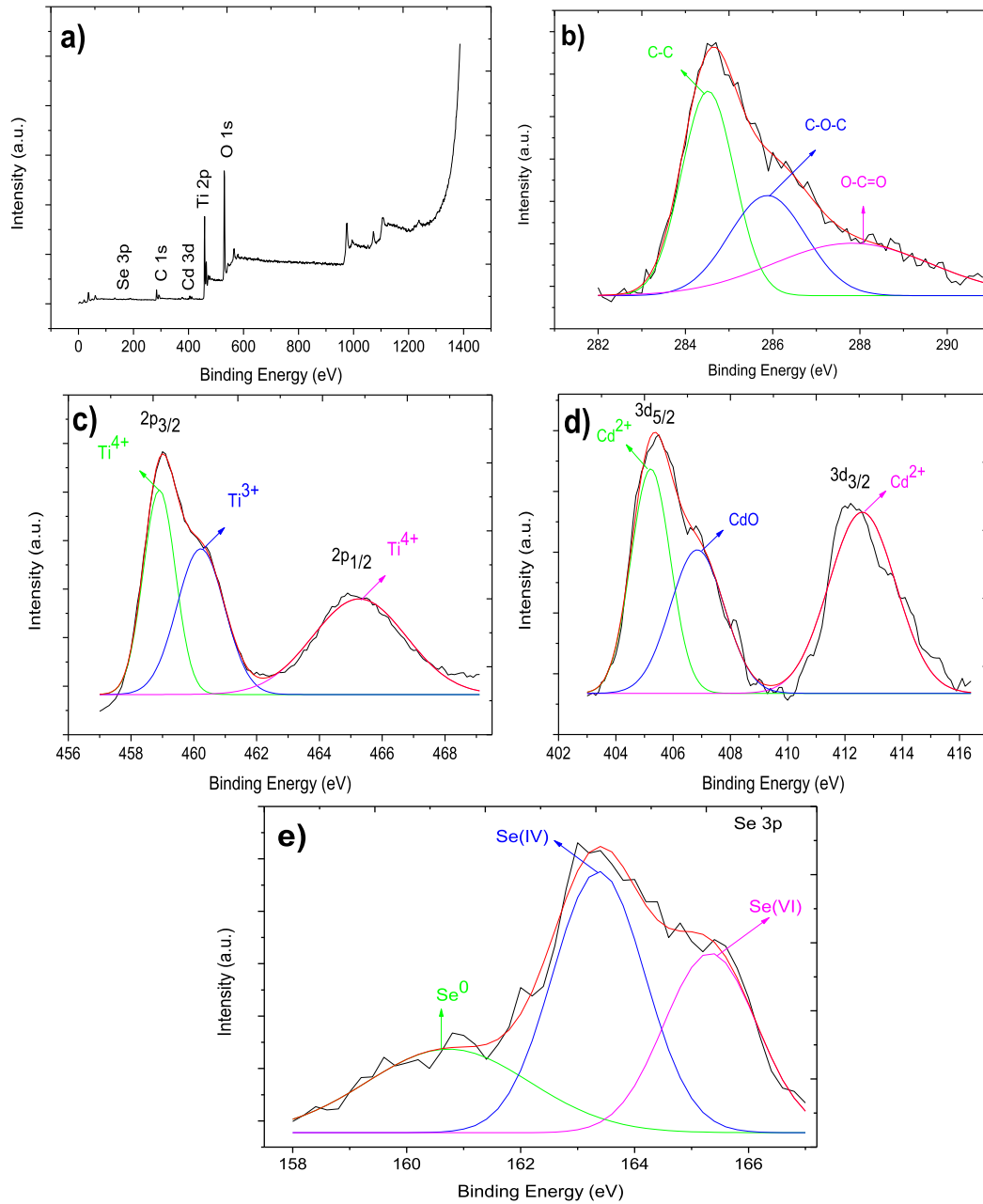
Fig. 5 – XPS spectra of (a) general spectrum (b) C 1s, (c) Ti 2p, (d) Cd 3d, (e) Se 3p for 0.1% CdSe(50-50)/TiO$_2$ catalyst.

**Table 5 – Probable chemical states in the XPS spectra of C 1s, Ti 2p, Cd 3d, and Se 3p regions.**

| Catalyst | Name | BE (eV) | Possible Chemical State | Relative Intensity % | Reference |
|---|---|---|---|---|---|
| 0.1% CdSe(50-50)/TiO$_2$ | C 1s | 284.5 | C—C | 45.39 | [59,60] |
| | | 285.9 | C—O—C | 30.74 | |
| | | 288.2 | O—C=O | 23.87 | |
| | Ti 2p | 458.9 | Ti$^{4+}$ | 43.20 | [67] |
| | | 460.2 | Ti$^{3+}$ | 33.39 | [62] |
| | | 465.3 | Ti$^{4+}$ | 23.41 | [68] |
| | Cd 3d | 405.2 | Cd$^{2+}$ | 35.72 | [69] |
| | | 406.8 | CdO | 31.08 | [65] |
| | | 412.5 | Cd$^{2+}$ | 33.20 | [70] |
| | Se 3p | 160.7 | Se$^0$ | 32.93 | [66] |
| | | 163.4 | Se(IV) | 33.72 | |
| | | 165.4 | Se(VI) | 33.35 | |

10 nm image is given in Fig. 4h. The particle size was about 4.8 nm. Many studies emphasized that the activity increased with the reduction in particle size [57,58]. EDX results revealed the presence of Cd, Se, Ti, and O metals. This result is equivalent to the SEM-EDX results.

Fig. 5a−e demonstrates the possible chemical states of Cd and Se in the 0.1% CdSe(50-50)/TiO$_2$ catalyst described by utilizing XPS analysis. All peak positions were defined relative to C 1s at a binding energy of 284.6 eV. The general spectrum for XPS analysis (Fig. 5a) of 0.1% CdSe(50-50)/TiO$_2$ catalyst illustrates peaks at C 1s, Ti 2p, O 1s, Cd 3d, and Se 3p. The C 1s with three different chemical shift components with binding energy of 284.5, 285.9, and 288.2 eV could be attributed to C−C, C−O−C, and O−C=O bonding [59,60]. From Fig. 5c, the Ti 2p spectrums with binding energy about 458.9 eV and 465.3 eV comprise Ti 2p$_{3/2}$ and Ti 2p$_{1/2}$ peaks showing the presence of Ti$^{4+}$ in TiO$_2$ lattice. Furthermore, the Ti 2p$_{1/2}$ peak at binding energy 460.2 eV is corresponding to Ti$^{3+}$ in Ti$_2$O$_3$ [61,62]. The binding energies at 405.2 eV and 412.5 eV of Cd 3d (Fig. 5d)

have two peaks at 3d$_{5/2}$ and 3d$_{3/2}$, which indicates the possible formation of Cd$^{2+}$ [63,64]. In addition, the binding energy of about 406.8 eV may be oxygen in the environment or Cd−O or Cd−Se−O complexes formed during the reduction process [65]. Fig. 5e indicates the binding energies of Se 3p. The binding energies at 160.7 eV, 163.4 eV, and 165.4 eV could be assigned to the Se$^0$, Se(IV), and Se(VI) bonds, respectively [66]. Furthermore, the probable chemical states of C 1s, Ti 2p, Cd 3d, and Se 3p for the 0.1% CdSe(50-50)/TiO$_2$ catalyst are summarized in Table 5.

The UV−visible diffuse reflectance spectrum was used to analyze the optical properties, one of the most important parameters for the photocatalytic activity of the TiO2 and CdSe/TiO$_2$ catalysts. Fig. 6a and b shows the UV−VIS absorbance spectra and the Tauc plots, respectively. As depicted in Fig. 6a, TiO$_2$ exhibited strong absorption under ultraviolet light with a wavelength at about 400 nm due to the band-gap of anatase-TiO$_2$. The preparation of TiO$_2$ with CdSe metals targeted changing the band-gap while remaining in the UV
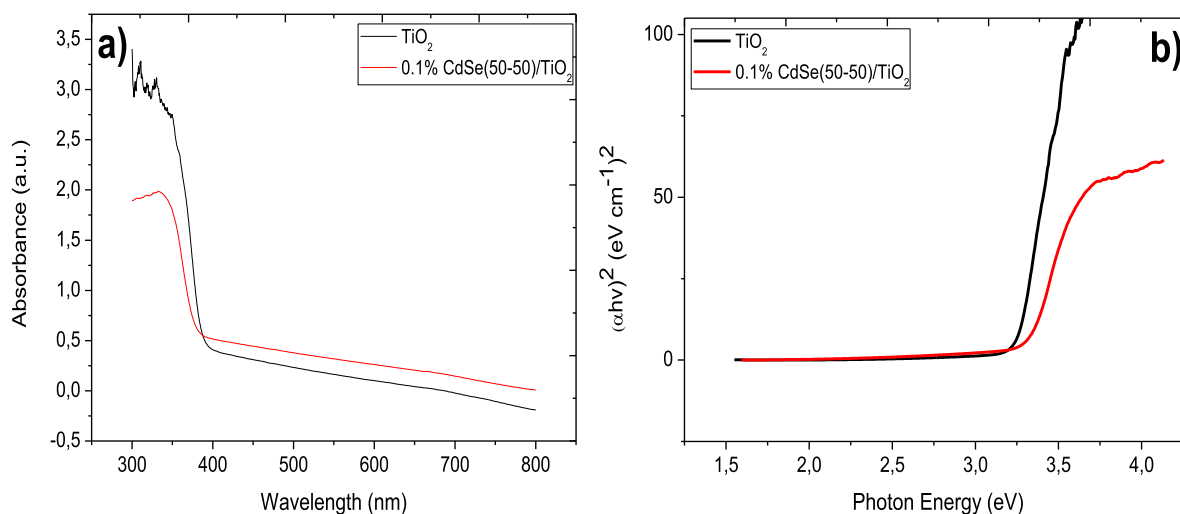
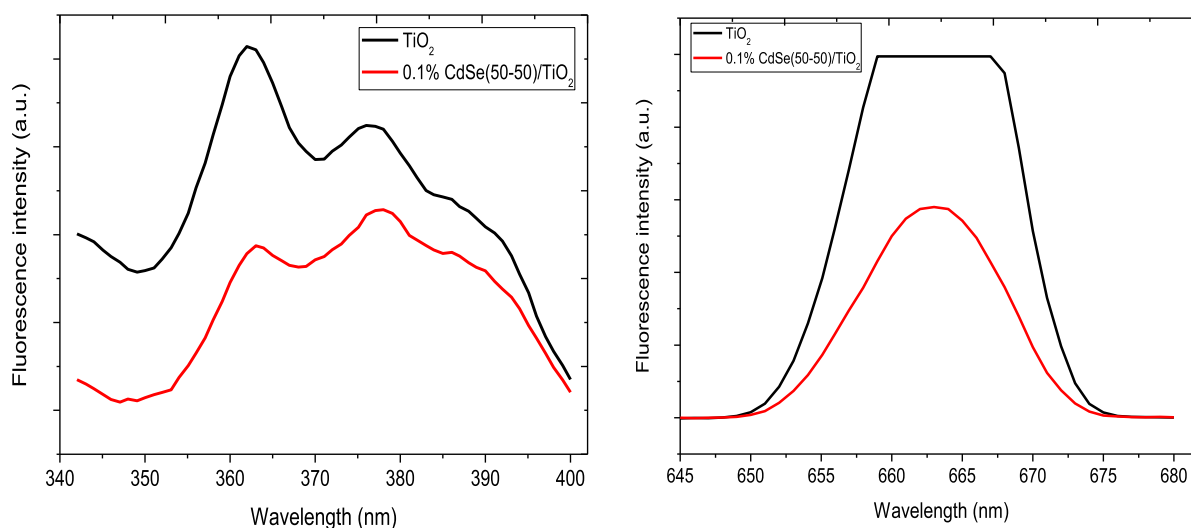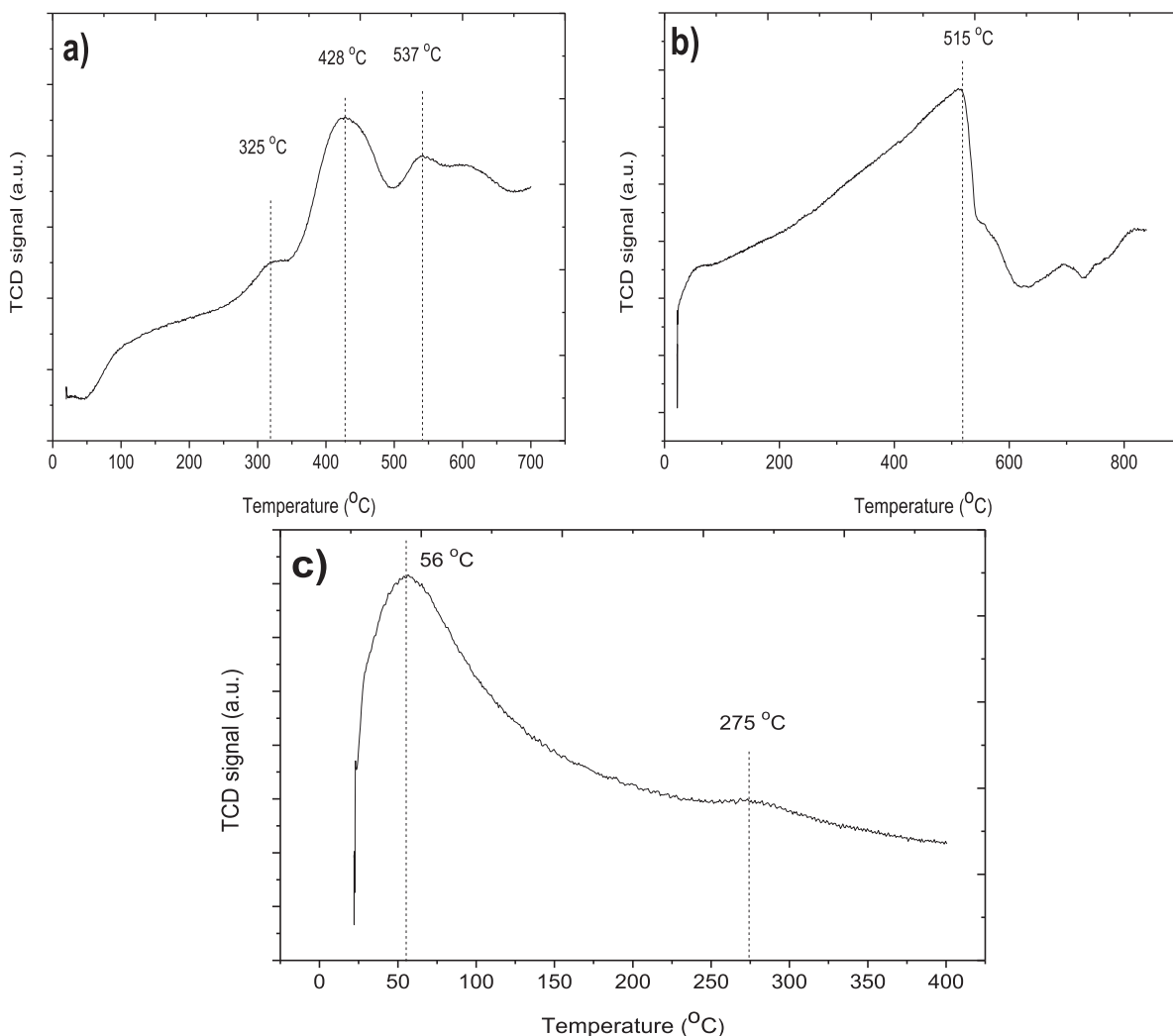**Fig. 6 − (a) UV-VIS absorbance spectrum and (b) Tauc plots for TiO$_2$ and 0.1% CdSe(50-50)/TiO$_2$ catalysts.**

**Fig. 7 − Fluorescence spectra of the TiO$_2$ and 0.1% CdSe(50-50)/TiO$_2$ catalysts.**

Fig. 8 – H$_2$-TPR a), O$_2$-TPO b), and NH$_3$-TPD c) profiles of 0.1% CdSe(50-50)/TiO$_2$ catalyst.

region and increasing the catalytic activity. Fig. 6a indicates that the absorption spectrum of CdSe(50-50)/TiO$_2$ stretched from 400 nm to 415 nm. As seen from Tauc plots in Fig. 6b, the band gap energies of the TiO$_2$ and CdSe/TiO$_2$ catalysts obtained from the formula $\lambda = 1240/Eg$ are 3.25 eV and 3.15 eV, respectively. These band-gap results illustrate that the introduction of CdSe into the TiO$_2$ structure results in an increase of the light absorption ability [71]. Furthermore, the addition of CdSe into TiO$_2$ demonstrates that it can effectively enhance the absorption of UV light for catalytic activity.

The fluorescence spectra of TiO$_2$ and 0.1% CdSe(50-50)/TiO$_2$ catalysts are given in Fig. 7. As a result of this analysis, the photocatalytic activity efficiency of the catalysts and the charge capturing properties of the semiconductor can be defined [72]. In Fig. 7, the peak density at approximately 363, 378, and 663 nm of the 0.1% CdSe(50-50)/TiO$_2$ catalyst was weaker than TiO$_2$. Fluorescence emission in semiconductor materials is mainly due to the recombination of photo-induced electrodes and holes [73]. Thus, the 0.1% CdSe(50-

50)/TiO$_2$ catalyst could effectively separate photo-induced electrons from the holes on the TiO$_2$ surface; therefore, making their recombination difficult and resulting in increased photocatalytic activity.

Fig. 8a–c shows the H$_2$-TPR, O$_2$-TPO, and NH$_3$-TPD analyses of 0.1% CdSe(50-50)/TiO$_2$ catalyst. H$_2$-TPR analysis was used to examine the behavior during reduction with hydrogen of the catalyst and the analysis result was illustrated in Fig. 8a. This analysis supplies information about the interaction between CdSe and TiO$_2$ due to the effects on the catalytic performance and properties of the catalyst when TiO$_2$ interacts with the metal [74]. TiO$_2$ and 0.1% Cd/TiO$_2$ catalysts underwent TPR, TPO, and TPD analyses in our previous study [75]. TPR profiles indicate the reduction behavior of metal oxides in catalysts under the same operating conditions. It can be seen from Fig. 8a that 0.1% CdSe(50-50)/TiO$_2$ catalyst has three peak TPR profiles at 325 °C, 428 °C, and 537 °C. The H$_2$-TPR analysis of TiO$_2$ was examined by many researchers in the literature and can be attributed to the peak TiO$_2$ or Ti$^{4+}$ reduction obtained at
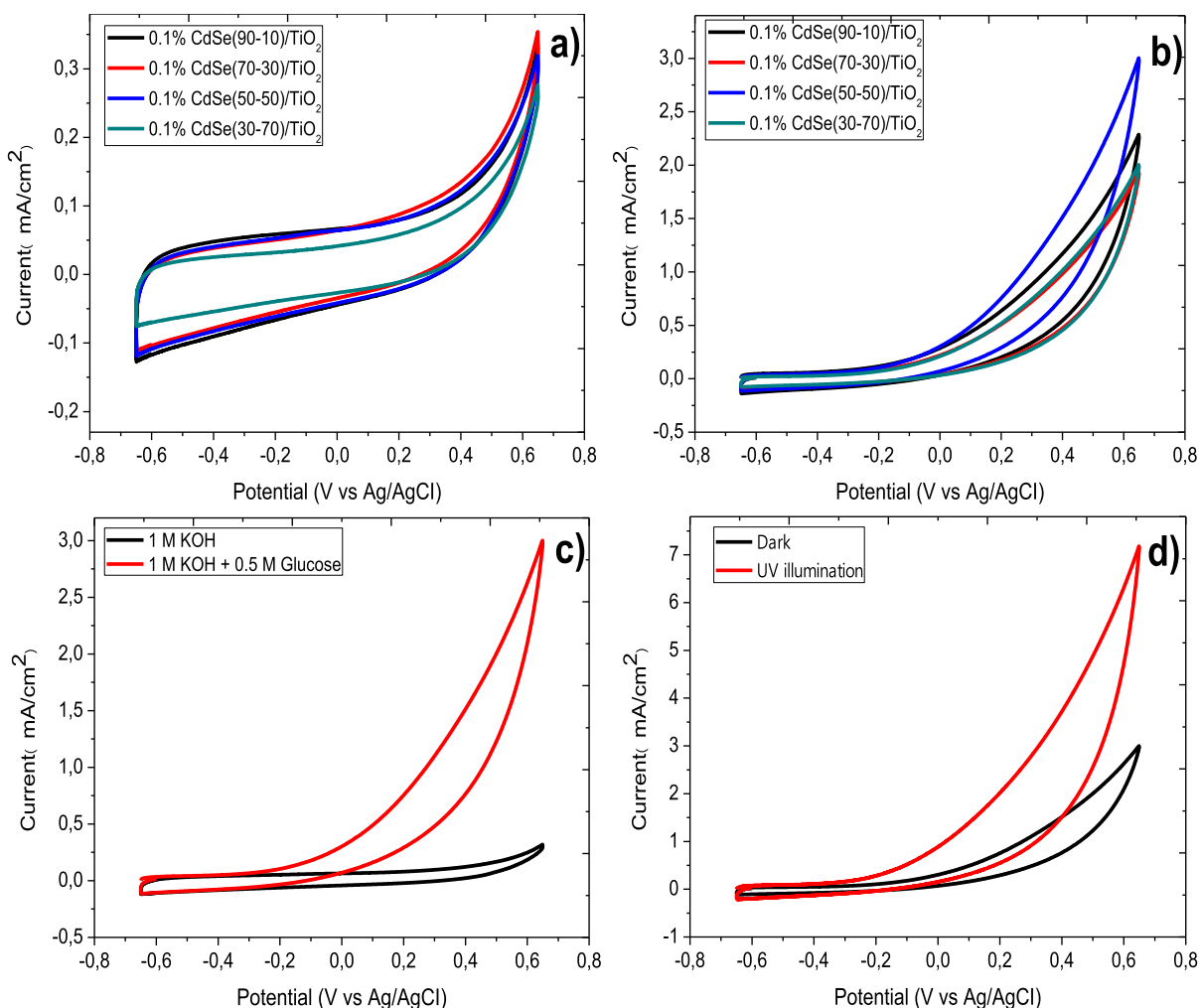
**Fig. 9 – Cyclic voltammograms for 0.1% CdSe/TiO₂ catalysts in (a) 1 M KOH, (b) 1 M KOH + 0.5 M glucose, (c) comparison of KOH and glucose for 0.1% CdSe(50-50)/TiO₂ catalyst, (d) in the dark and under UV illumination of 0.1% CdSe(50-50)/TiO₂ catalyst at 100 mV s⁻¹ scan rate.**

**Table 6 – Electrochemical behaviors of 0.1% CdSe/TiO₂ catalysts in the dark for glucose electrooxidation.**

| Sample | Total current (mA/cm²) | | | Mass Activity (mA/mg Cd) | Onset Potential (V) |
|---|---|---|---|---|---|
| | KOH | Glucose | Normal | | |
| 0.1% CdSe(90–10)/TiO₂ | 0.33 | 2.26 | 1.93 | 4830.31 | −0.38 |
| 0.1% CdSe(70–30)/TiO₂ | 0.35 | 1.94 | 1.59 | 3980.17 | −0.35 |
| 0.1% CdSe(50–50)/TiO₂ | 0.31 | 3.02 | 2.71 | 6786.54 | −0.35 |
| 0.1% CdSe(30–70)/TiO₂ | 0.27 | 2.00 | 1.73 | 4336.49 | −0.32 |

approximately 400–750 °C [76]. Therefore, the TPR profile at 537 °C can be attributed to the reduction peak of TiO₂. When TiO₂ is doped with CdSe metal, its reducibility increases, and therefore the reduction temperatures decrease. The peaks formed at 325 °C and 428 °C indicate that the reducibility of TiO₂ decreased due to CdSe metals. The O₂-TPO analysis of 0.1% CdSe(50-50)/TiO₂ catalyst is shown in Fig. 8b. TPO analysis is a material characterization process that involves heating to a certain temperature by passing an oxidizing gas mixture containing oxygen over the sample and then forming oxidation with the thermal excitation that occurs. It can be

observed from Fig. 8b that TiO₂ and 0.1% CdSe(50-50)/TiO₂ catalyst have sharp peaked TPO profiles at 785 °C [75] and 515 °C, respectively. When doped with Cd and Se metals, the metals are oxidized before the support material and the oxidation temperature decreases due to the metal support [77]. TPD analysis is used to characterize the adsorption sites on the sample with an inert gas mixture of gases such as NH₃ and CO₂, which examines the events occurring on the surface of solid samples with temperature changed by a temperature program. This analysis primarily involves measuring the rate of adsorption at the sample surface at low temperatures with
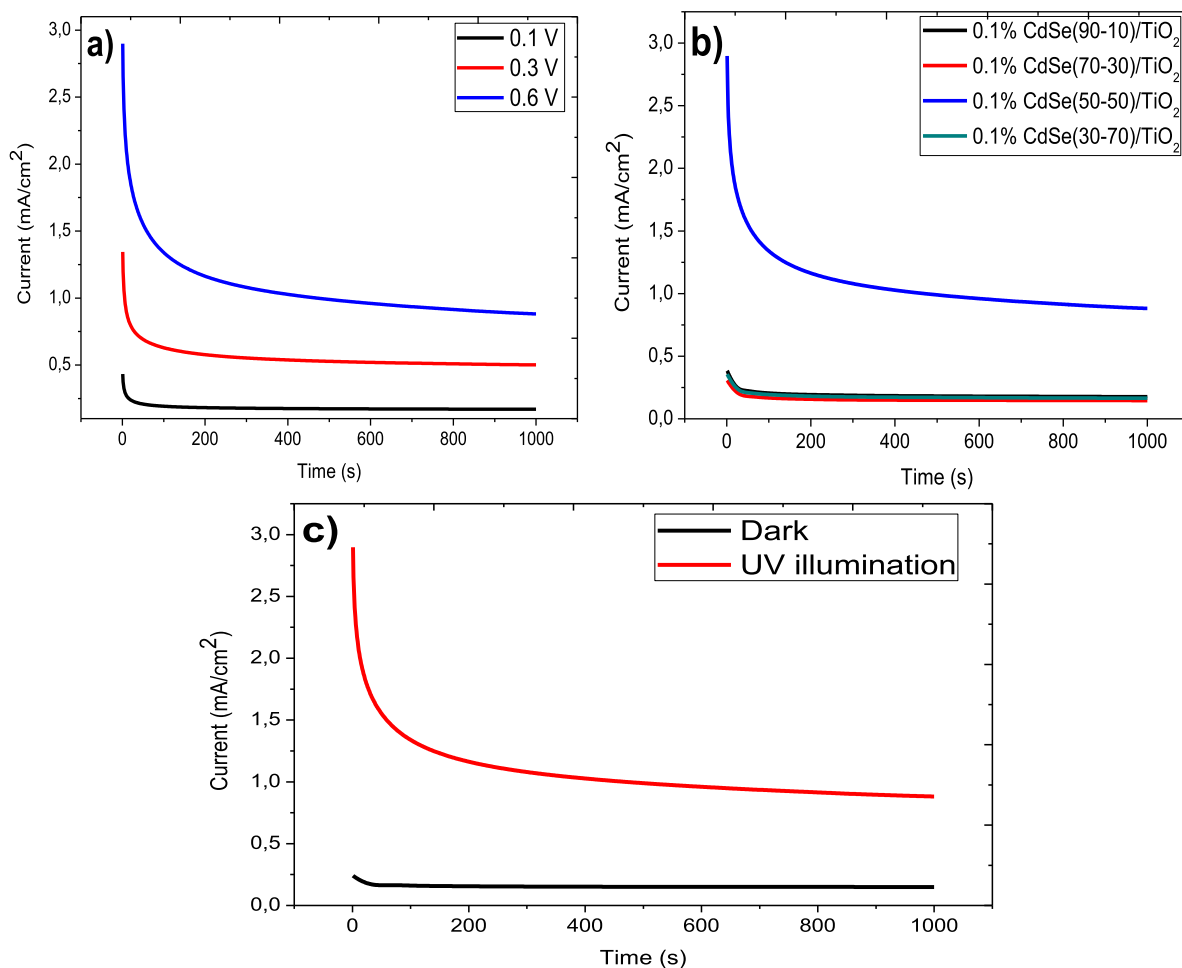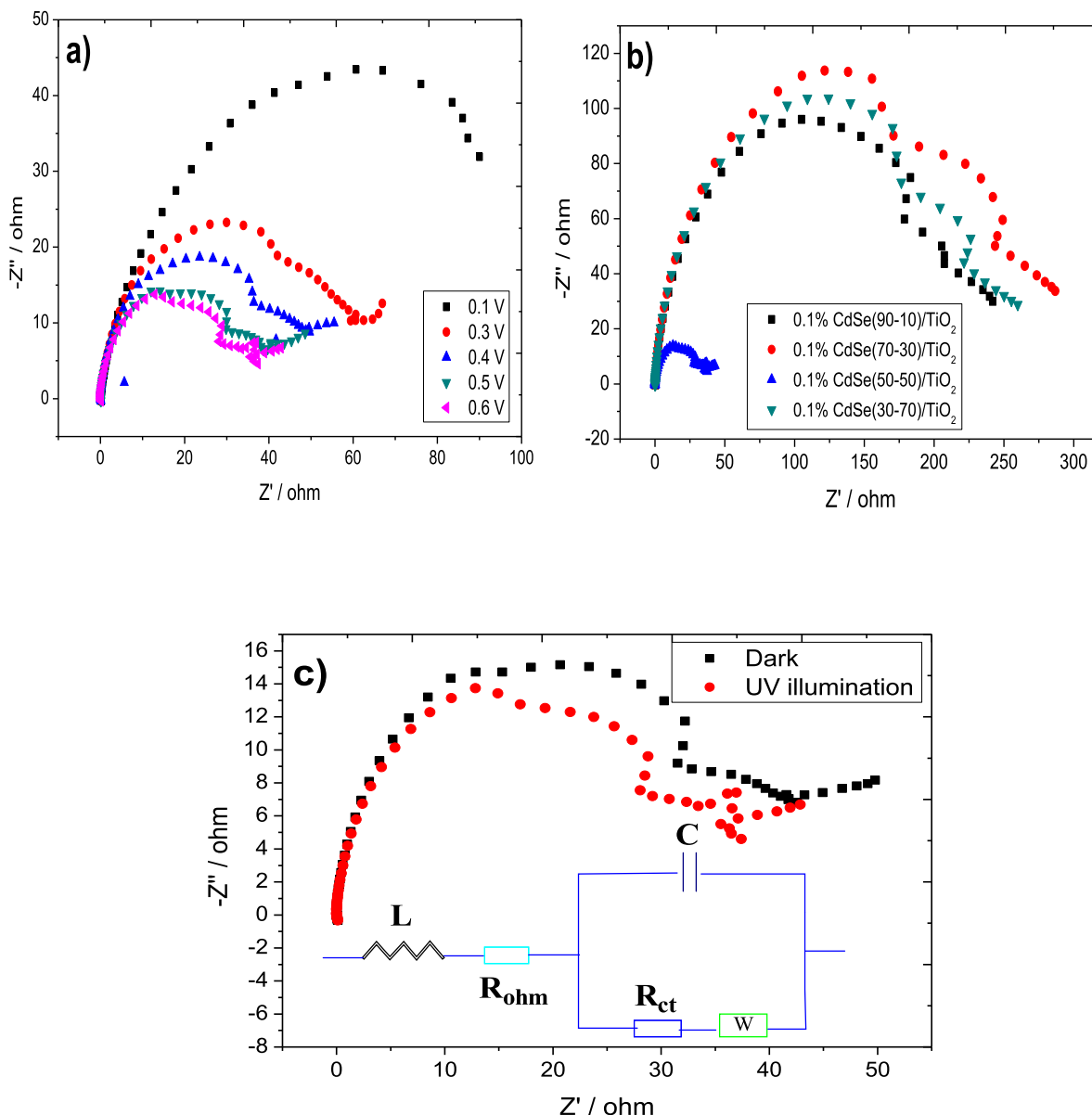
**Fig. 10 − CA curves of (a) 0.1% CdSe(50-50)/TiO$_2$ under UV illumination at different potentials, (b) 0.1% CdSe/TiO$_2$ catalysts under UV illumination at 0.6 V, (c) 0.1% CdSe(50-50)/TiO$_2$ in the dark and under UV illumination at 0.6 V in 1 M KOH + 0.5 M glucose solution.**

a known gas and inert gas mixture, and the rate of desorption as the temperature increases [78]. The NH$_3$-TPD curves for 0.1% CdSe(50-50)/TiO$_2$ catalyst are shown in Fig. 8c. TPD curves indicate the changing acidic state of the sample as the temperature increases, as weak acid, medium acid, and strong acid [79,80]. While the peaks assigned to physical adsorption for the TiO$_2$ catalyst were at about 56 °C, they were about 275 °C for CdSe/TiO$_2$. The peak area increased when TiO$_2$ was doped with metal. Furthermore, this peak for the CdSe/TiO$_2$ catalyst is attributed to the desorption of weakly-bound NH$_3$ corresponding to medium-strength acid sites resulting from the desorption of NH$_3$ at Lewis or strong Brønsted acid sites [81].

*Electrochemical measurements of CdSe/TiO$_2$ catalysts*

The CdSe/TiO$_2$ catalysts were used with glucose as fuel to examine their photocatalytic performances. CV, CA, and EIS analyses were performed to investigate the catalytic activity, stability, and resistance of catalysts, respectively. These analyses were obtained in the dark and under UV illumination in 1 M KOH + 0.5 M glucose solution. Fig. 9a−d illustrates PGE of

catalysts in the dark and under UV illumination. The electrochemical behaviors of 0.1% CdSe/TiO$_2$ catalysts were examined with CV analysis between −0.65 and 0.65 V potential with a scan rate of 100 mV s$^{-1}$ in 1 M KOH and 1 M KOH + 0.5 M glucose solution (Fig. 9a and b). Table 6 shows the catalytic activities of the CdSe/TiO$_2$ catalysts at total current values in the dark in the KOH and glucose solution. Although glucose has high energy density, it is a difficult fuel to break down. Therefore, the catalysts were evaluated over the total current because oxidation peaks did not occur in glucose electrooxidation measurements. Fig. 9b shows that the 0.1% CdSe(50-50)/TiO$_2$ catalyst displayed the best catalytic activity compared to the others, with specific activity at the total current (glucose) of 2.71 mA/cm$^2$ (6786.54 mA/mg Cd) in the dark. Fig. 9c shows a comparison of 0.1% CdSe(50-50)/TiO$_2$ catalyst with 1 M KOH and 1 M KOH + 0.5 M glucose. The 2.71 mA/cm$^2$ specific activity occurring in the total current is the catalytic activity originating from glucose. The 0.1% CdSe(50-50)/TiO$_2$ catalyst was examined for PGE under UV illumination (Fig. 9d). The 0.1% CdSe(50-50)/TiO$_2$ catalyst exhibited approximately 2.7 time better catalytic activity with an onset potential of −0.40 V (Ag/AgCl) and specific activity of

**Fig. 11 — Nyquist plots of (a) 0.1% CdSe(50-50)/TiO₂ under UV illumination at different potentials, (b) Comparison of 0.1% CdSe/TiO₂ catalysts under UV illumination at 0.6 V, (c) 0.1% CdS(50-50)/TiO₂ catalyst in the dark and under UV illumination at 0.6 V in 1 M KOH + 0.5 M glucose solution.**

7.20 mA/cm² (18030.65 mA/mg Cd) under UV illumination compared to dark conditions. Furthermore, it exhibited better photocatalytic activity under UV illumination compared to 0.1% Cd/TiO₂ (6.00 mA/cm²) [75] in our previous study. Though it includes a small amount of metal compared to the literature, it is a promising photoanode for PFCs with high specific and mass activity.

CA analysis was used to evaluate the stability and poison resistance of CdSe/TiO₂ catalysts. Fig. 10a—c demonstrates the CA curves of catalysts. CA analysis of 0.1% CdSe(50-50)/TiO₂ catalyst was performed at different potentials (0.1 V, 0.3, and 0.6 V) under UV illumination (Fig. 10a). CA analysis at 0.6 V potential exhibited the best resistance and stability. After 1000 s, 0.1% CdSe(50-50)/TiO₂ catalyst had better activity and

stability with 0.90 mA/cm² specific activity compared to other catalysts under UV illumination at 0.6 V potential (Fig. 10b). Fig. 10c show that the 0.1% CdSe(50-50)/TiO₂ catalyst under UV illumination was more stable than in the dark (0.15 mA/cm²). As with the CV results, 0.1% CdSe(50-50)/TiO₂ catalyst exhibited the best activity and stability compared to values in the dark and the other atomic molar ratios.

Fig. 11a—d show the Nyquist plots obtained from EIS analysis to investigate the electrocatalytic resistance of the 0.1% CdSe/TiO₂ catalysts. These plots are usually known as semicircles, where the electrocatalytic resistance increases as the diameter of the circle decreases [82,83]. The charge transfer resistance ($R_{ct}$) is associated with the diameter of the semicircle because as the diameter decreases, $R_{ct}$ decreases,

and so the catalytic activity increases [84]. Fig. 11a demonstrates the Nyquist plots for 0.1% CdSe(50-50)/TiO$_2$ under UV illumination at different potentials (0.1 V, 0.3 V, 0.4 V, 0.5 V, and 0.6 V). As shown in Fig. 11a, the Nyquist plot at the potential of 0.6 V displayed the best photocatalytic activity. Fig. 11b shows the Nyquist plots for 0.1% CdSe(90—10)/TiO$_2$ (1720.0 Ω), 0.1% CdSe(70—30)/TiO$_2$ (2034.0 Ω), 0.1% CdSe(50-50)/TiO$_2$ (289.1 Ω), 0.1% CdSe(30—70)/TiO$_2$ (1900.0 Ω) catalysts. Fig. 11b clear show that 0.1% CdSe(50-50)/TiO$_2$ catalyst had a much smaller R$_{ct}$ value compared to other atomic molar ratios. In addition, Fig. 11c shows the Nyquist plot in the dark and under UV illumination for 0.1% CdSe(50-50)/TiO$_2$ catalyst at 0.6 V. It can be seen from Fig. 11c that the R$_{ct}$ of 0.1% CdSe(50-50)/TiO$_2$ under UV illumination is much smaller compared to the value in the dark (329.6 Ω), indicating faster electron transfer rate and higher catalytic activity during photocatalytic glucose electrooxidation. The equivalent circuit was proposed as depicted in the inset of Fig. 11c where R$_{ohm}$ is cell ohmic resistance, R$_{ct}$ is electrochemical kinetic-related resistance, C$_{dl}$ is the double-layer capacitance corresponding to charge storage at the interface between the electrolyte and electrode, and L is the adsorption inductance [85,86].

## Conclusion

The wetness impregnation method was utilized to prepare TiO$_2$-supported CdSe catalysts with different atomic molar ratios (90—10, 70—30, 50-50, and 30—70). XRD, SEM-EDX, TEM, XPS, UV-VIS spectroscopy, fluorescence spectroscopy, TPR, TPO, and TPD analyses were completed to characterize the catalysts. The XRD results revealed that only anatase-TiO$_2$ structures formed because a very low amount of CdSe metal was used. This shows that the metals were well dispersed within TiO$_2$ [50]. SEM-EDX and mapping and TEM-EDS results indicated that anatase-TiO$_2$ and CdSe metal particles had formed. In addition, CdSe particles had a particle size of 4.8 nm and were homogeneously dispersed. 0.1% CdSe(50-50)/TiO$_2$ catalyst had the highest surface area and lowest pore and nanoparticle size compared to other catalysts. As the surface area increases, the interaction between the reactant and catalyst atoms/molecules increases. Therefore, the reaction rate increases due to the increase in intermolecular collisions. As a result, catalysts with a large surface area have high catalytic activity. XPS analysis illustrated the changes in the crystal structure and electronic state of the samples. The UV-VIS spectrum showed that the bandgap of CdSe/TiO$_2$ relative to TiO$_2$ decreased but still remained in the UV region. TPR, TPO, and TPD analyses presented positive or negative shifts in the reduction, oxidation, and adsorption-desorption peaks of TiO$_2$ when the temperature increased after doping with metal, indicating the presence of metal. CV, CA, and EIS analyses were performed to examine the activity, stability, and resistance for PGE measurements of 0.1% CdSe/TiO$_2$ catalysts in the dark and under UV illumination, respectively. The 0.1% CdSe(50-50)/TiO$_2$ catalyst under UV illumination displayed the best photocatalytic activity with a specific activity of 7.20 mA/cm$^2$ (18030.65 mA/mg Cd) compared to experiments in the dark with 2.71 mA/cm$^2$ (6786.54 mA/mg Cd) and other

catalysts. It also had the best stability and resistance for photocatalytic glucose electrooxidation according to CA and EIS analyses under UV illumination as in the CV analysis. The catalytic activity increased due to the synergistic effect between Cd and Se [83]. The reason why 0.1% CdSe(50-50)/TiO$_2$ catalyst exhibits the best catalytic activity compared to other metal ratios is that the ratios are close to each other, preventing the Se metal from reducing its activity by coating the Cd surface and increasing the synergistic effect between them. Furthermore, the crystallite size, micro-strain, and dislocation density obtained from XRD analysis confirmed the high activity of this catalyst. There are very few studies in the literature about PGE. 0.1% CdSe(50-50)/TiO$_2$ catalyst had high catalytic activity for PGE and glucose electrooxidation compared to the literature. These results are promising for its use as a photoanode catalyst for PFCs with low metal content and high specific and mass photoactivity.

## Declaration of competing interest

The authors declare that they have no known competing financial interests or personal relationships that could have appeared to influence the work reported in this paper.

## Acknowledgment

## Appendix A. Supplementary data

Supplementary data to this article can be found online at https://doi.org/10.1016/j.ijhydene.2022.04.231.

REFERENCES

[1] Asongu SA, Agboola MO, Alola AA, Bekun FV. The criticality of growth, urbanization, electricity and fossil fuel consumption to environment sustainability in Africa. Sci Total Environ 2020;712:136376.

[2] Chen Y-H, Chen C-Y, Lee S-C. Technology forecasting and patent strategy of hydrogen energy and fuel cell technologies. Int J Hydrogen Energy 2011;36:6957—69.

[3] Jain IP. Hydrogen the fuel for 21st century. Int J Hydrogen Energy 2009;34:7368—78.

[4] Suha Yazici M. Hydrogen and fuel cell activities at UNIDO-ICHET. Int J Hydrogen Energy 2010;35:2754—61.

[5] Galińska A, Walendziewski J. Photocatalytic water splitting over Pt—TiO2 in the presence of sacrificial reagents. Energy Fuels 2005;19:1143—7.

[6] Caglar A, Sahan T, Cogenli MS, Yurtcan AB, Aktas N, Kivrak H. A novel Central Composite Design based response surface methodology optimization study for the synthesis of Pd/CNT direct formic acid fuel cell anode catalyst. Int J Hydrogen Energy 2018;43:11002—11.

[7] Ma Z, Liu J, Zhu Y, Zhao Y, Lin H, Zhang Y, Li H, Zhang J, Liu Y, Gao W, Li S, Li L. Crystal-facet-dependent catalysis of

anatase TiO2 on hydrogen storage of MgH2. J Alloys Compd 2020;822:153553.

[8] Akdemir M, Avci Hansu T, Caglar A, Kaya M, Demir Kivrak H. Ruthenium modified defatted spent coffee catalysts for supercapacitor and methanolysis application. Energy Storage 2021;3:e243.

[9] Reeves P, Ohlhausen R, Sloan D, Pamplin K, Scoggins T, Clark C, Hutchinson B, Green D. Photocatalytic destruction of organic dyes in aqueous TiO2 suspensions using concentrated simulated and natural solar energy. Sol Energy 1992;48:413—20.

[10] Pinilla S, Machín A, Park S-H, Arango JC, Nicolosi V, Márquez-Linares F, Morant C. TiO2-Based nanomaterials for the production of hydrogen and the development of lithium-ion batteries. J Phys Chem B 2018;122:972—83.

[11] Eshghi A, kheirmand M. Graphene/Ni—Fe layered double hydroxide nano composites as advanced electrode materials for glucose electro oxidation. Int J Hydrogen Energy 2017;42:15064—72.

[12] Caglar A, Kivrak H. Highly active carbon nanotube supported PdAu alloy catalysts for ethanol electrooxidation in alkaline environment. Int J Hydrogen Energy 2019;44:11734—43.

[13] Reyes-Valenzuela M, Sánchez-Squella A, Barraza R, Osses M, Valdivia-Lefort P. Economic evaluation of fuel cell-powered OFF-ROAD machinery using stochastic analysis. Int J Hydrogen Energy 2022;47:2771—82.

[14] Durai L, Gunasekaran SS, Badhulika S. A non-noble, low cost, multicomponent electrocatalyst based on nickel oxide decorated AC nanosheets and PPy nanowires for the direct methanol oxidation reaction. Int J Hydrogen Energy 2022;47:3099—107.

[15] Galvagno A, Chiodo V, Urbani F, Freni F. Biogas as hydrogen source for fuel cell applications. Int J Hydrogen Energy 2013;38:3913—20.

[16] Li X, Wang G, Jing L, Ni W, Yan H, Chen C, Yan Y-M. A photoelectrochemical methanol fuel cell based on aligned TiO2 nanorods decorated graphene photoanode. Chem Commun 2016;52:2533—6.

[17] Han L, Guo S, Xu M, Dong S. Photoelectrochemical batteries for efficient energy recovery. Chem Commun 2014;50:13331—3.

[18] Zhao Q, Li Z, Deng Q, Zhu L, Luo S, Li H. Paired photoelectrocatalytic reactions of glucose driven by a photoelectrochemical fuel cell with assistance of methylene blue. Electrochim Acta 2016;210:38—44.

[19] Dong F, Liu X, Irfan M, Yang L, Li S, Ding J, Li Y, Khan IU, Zhang P. Macaroon-like FeCo2O4 modified activated carbon anode for enhancing power generation in direct glucose fuel cell. Int J Hydrogen Energy 2019;44:8178—87.

[20] Gao M, Liu X, Irfan M, Shi J, Wang X, Zhang P. Nickle-cobalt composite catalyst-modified activated carbon anode for direct glucose alkaline fuel cell. Int J Hydrogen Energy 2018;43:1805—15.

[21] Elouarzaki K, Le Goff A, Holzinger M, Thery J, Cosnier S. Electrocatalytic oxidation of glucose by rhodium porphyrin-functionalized MWCNT electrodes: application to a fully molecular catalyst-based glucose/O2 fuel cell. J Am Chem Soc 2012;134:14078—85.

[22] Caglar A, Ulas B, Sahin O, Demir Kivrak H. Few-layer graphene coated on indium tin oxide electrodes prepared by chemical vapor deposition and their enhanced glucose electrooxidation activity. Energy Storage 2019;1:e73.

[23] Caglar A, Ulas B, Sahin O, Kıvrak H. Synthesis of in situ N-, S-, and B-doped few-layer graphene by chemical vapor deposition technique and their superior glucose electrooxidation activity. Int J Energy Res 2019;43:8204—16.

[24] Caglar A, Düzenli D, Onal I, Tezsevin I, Sahin O, Kivrak H. A comparative experimental and density functional study of glucose adsorption and electrooxidation on the Au-graphene and Pt-graphene electrodes. Int J Hydrogen Energy 2020;45:490—500.

[25] Caglar A, Düzenli D, Onal I, Tezsevin I, Sahin O, Kivrak H. A novel experimental and density functional theory study on palladium and nitrogen doped few layer graphene surface towards glucose adsorption and electrooxidation. J Phys Chem Solid 2021;150:109684.

[26] Brouzgou A, Song S, Tsiakaras P. Carbon-supported PdSn and Pd3Sn2 anodes for glucose electrooxidation in alkaline media. Appl Catal, B: Environ 2014;158—159:209—16.

[27] Lu S-J, Ji S-B, Liu J-C, Li H, Li W-S. Photoelectrocatalytic oxidation of glucose at a ruthenium complex modified titanium dioxide electrode promoted by uric acid and ascorbic acid for photoelectrochemical fuel cells. J Power Sources 2015;273:142—8.

[28] Ameta R, Solanki MS, Benjamin S, Ameta SC. Chapter 6 - photocatalysis. In: Ameta SC, Ameta R, editors. Advanced Oxidation Processes for Waste Water Treatment. Academic Press; 2018. p. 135—75.

[29] Matsumoto Y. Energy positions of oxide semiconductors and photocatalysis with iron complex oxides. J Solid State Chem 1996;126:227—34.

[30] Nishanthi S, Raja DH, Subramanian E, Padiyan DP. Remarkable role of annealing time on anatase phase titania nanotubes and its photoelectrochemical response. Electrochim Acta 2013;89:239—45.

[31] Fujishima A, Honda K. Electrochemical photolysis of water at a semiconductor electrode. Nature 1972;238:37—8.

[32] Chiarello GL, Dozzi MV, Selli E. TiO2-based materials for photocatalytic hydrogen production. J Energy Chem 2017;26:250—8.

[33] Zheng L, Teng F, Ye X, Zheng H, Fang X. Photo/electrochemical applications of metal sulfide/TiO2 heterostructures. Adv Energy Mater 2020;10:1902355.

[34] Pan B, Qin J, Wang C. 6 - photoreduction of CO2 on non-TiO2—based metal oxides. In: Wang X, Anpo M, Fu X, editors. Current Developments in Photocatalysis and Photocatalytic Materials. Elsevier; 2020. p. 77—87.

[35] Kuvarega AT, Mamba BB. TiO2-based photocatalysis: toward visible light-responsive photocatalysts through doping and fabrication of carbon-based nanocomposites. Crit Rev Solid State Mater Sci 2017;42:295—346.

[36] Wang C, Thompson RL, Baltrus J, Matranga C. Visible light photoreduction of CO2 using CdSe/Pt/TiO2 heterostructured catalysts. J Phys Chem Lett 2010;1:48—53.

[37] Ghosh T, Ullah K, Nikam V, Park C-Y, Meng Z-D, Oh W-C. The characteristic study and sonocatalytic performance of CdSe—graphene as catalyst in the degradation of azo dyes in aqueous solution under dark conditions. Ultrason Sonochem 2013;20:768—76.

[38] Meng P, Wang M, Yang Y, Zhang S, Sun L. CdSe quantum dots/molecular cobalt catalyst co-grafted open porous NiO film as a photocathode for visible light driven H2 evolution from neutral water. J Mater Chem 2015;3:18852—9.

[39] Hu C, Kelm D, Schreiner M, Wollborn T, Mädler L, Teoh WY. Designing photoelectrodes for photocatalytic fuel cells and elucidating the effects of organic substrates. ChemSusChem 2015;8:4005—15.

[40] Chu D, Li XH, Feng DX, Gu JS, Shen G. Electrocatalytic oxidation of glucose on carbon nanotube/nanocrystalline TiO2 film loaded Pt complex electrode. Hua Hsueh Hsueh Pao 2004;62:2403—6.

[41] Gu Y, Yang H, Li B, Mao J, An Y. A ternary nanooxide NiO-TiO2-ZrO2/SO42− as efficient solid superacid catalysts for electro-oxidation of glucose. Electrochim Acta 2016;194:367—76.

[42] Long M, Tan L, Tang AD. The effects of electroplating conditions on the morphology and glucose oxidation performance of Cu2O/TiO2. Adv Mater Res 2014;937:3—8.

[43] Gu Y, Liu Y, Yang H, Li B, An Y. Electrocatalytic glucose oxidation via hybrid nanomaterial catalyst of multi-wall TiO2 nanotubes supported Ni(OH)2 nanoparticles: optimization of the loading level. Electrochim Acta 2015;160:263—70.

[44] Caglar A, Kivrak H, Aktas N, Solak AO. Fabrication of carbon-doped titanium dioxide nanotubes as anode materials for photocatalytic glucose fuel cells. J Electron Mater 2021:1—12.

[45] Trang TNQ, Nam ND, Ngoc Tu LT, Quoc HP, Van Man T, Ho VTT, Thu VTH. In situ spatial charge separation of an Ir@TiO2 multiphase photosystem toward highly efficient photocatalytic performance of hydrogen production. J Phys Chem C 2020;124:16961—74.

[46] Xiong Z, Lei Z, Li Y, Dong L, Zhao Y, Zhang J. A review on modification of facet-engineered TiO2 for photocatalytic CO2 reduction. J Photochem Photobiol C Photochem Rev 2018;36:24—47.

[47] Li W, Zhang M, Du Z, Ma Q, Jameel H, Chang H-m. Photocatalytic degradation of lignin model compounds and kraft pine lignin by CdS/TiO2 under visible light irradiation. Bioresources 2015;10:1245—59.

[48] Qu X, Liu M, Li L, Wang R, Sun H, Shi L, Du F. BiOBr flakes decoration and structural modification for CdTe/TiO2 spheres: towards water decontamination under simulated light irradiation. Mater Sci Semicond Process 2019;93:331—8.

[49] Liu L, Hensel J, Fitzmorris RC, Li Y, Zhang JZ. Preparation and photoelectrochemical properties of CdSe/TiO2 hybrid mesoporous structures. J Phys Chem Lett 2010;1:155—60.

[50] Huang K, Chen L, Deng J, Xiong J. Enhanced visible-light photocatalytic performance of nanosized anatase TiO$_2$ doped with CdS quantum dots for cancer-cell treatment. J Nanomater 2012;2012:720491.

[51] Kite SV, Kadam AN, Sathe DJ, Patil S, Mali SS, Hong CK, Lee SW, Garadkar KM. Nanostructured TiO2 sensitized with MoS2 nanoflowers for enhanced photodegradation efficiency toward methyl orange. ACS Omega 2021;6:17071—85.

[52] Pawar RA, Dubal DP, Kite SV, Garadkar KM, Bhuse VM. Photoelectrochemical and photocatalytic activity of nanocrystalline TiO2 thin films deposited by chemical bath deposition method. J Mater Sci Mater Electron 2021;32:19676—87.

[53] Nyathi TM, Fischer N, York APE, Claeys M. Effect of crystallite size on the performance and phase transformation of Co3O4/Al2O3 catalysts during CO-PrOx − an in situ study. Faraday Discuss 2017;197:269—85.

[54] Bensaid S, Piumetti M, Novara C, Giorgis F, Chiodoni A, Russo N, Fino D. Catalytic oxidation of CO and soot over Ce-Zr-Pr mixed oxides synthesized in a multi-inlet vortex reactor: effect of structural defects on the catalytic activity. Nanoscale Res Lett 2016;11:494.

[55] Chu S, Zhou W, Zhang C, Zheng Y, Liu Y, Liu Y. Relationship between the structure and catalytic performance of MoS 2 with different surfactant-assisted syntheses in the hydrodesulfurization reaction of 4, 6-DMDBT. RSC Adv 2020;10:7600—8.

[56] Gholap H, Patil R, Yadav P, Banpurkar A, Ogale S, Gade W. CdTe-TiO2 nanocomposite: an impeder of bacterial growth and biofilm. Nanotechnology 2013;24:195101.

[57] Kim DS, Han SJ, Kwak S-Y. Synthesis and photocatalytic activity of mesoporous TiO2 with the surface area, crystallite size, and pore size. J Colloid Interface Sci 2007;316:85—91.

[58] Jiang C, Wei M, Qi Z, Kudo T, Honma I, Zhou H. Particle size dependence of the lithium storage capability and high rate performance of nanocrystalline anatase TiO2 electrode. J Power Sources 2007;166:239—43.

[59] Wu Y, Lin Y, Xu J. Synthesis of Ag—Ho, Ag—Sm, Ag—Zn, Ag—Cu, Ag—Cs, Ag—Zr, Ag—Er, Ag—Y and Ag—Co metal organic nanoparticles for UV-Vis-NIR wide-range bio-tissue imaging. Photochem Photobiol Sci 2019;18:1081—91.

[60] Xiao S, Xu P, Peng Q, Chen J, Huang J, Wang F, Noor N. Layer-by-layer assembly of polyelectrolyte multilayer onto PET fabric for highly tunable dyeing with water soluble dyestuffs. Polymers 2017;9:735.

[61] Bharti B, Kumar S, Lee H-N, Kumar R. Formation of oxygen vacancies and Ti 3+ state in TiO 2 thin film and enhanced optical properties by air plasma treatment. Sci Rep 2016;6:1—12.

[62] Xie W, Li R, Xu Q. Enhanced photocatalytic activity of Se-doped TiO2 under visible light irradiation. Sci Rep 2018;8.

[63] Li W, Li M, Xie S, Zhai T, Yu M, Liang C, Ouyang X, Lu X, Li H, Tong Y. Improving the photoelectrochemical and photocatalytic performance of CdO nanorods with CdS decoration. CrystEngComm 2013;15:4212—6.

[64] Li Y-S, Jiang F-L, Xiao Q, Li R, Li K, Zhang M-F, Zhang A-Q, Sun S-F, Liu Y. Enhanced photocatalytic activities of TiO2 nanocomposites doped with water-soluble mercapto-capped CdTe quantum dots. Appl Catal B Environ 2010;101:118—29.

[65] Zeng C, Ramos-Ruiz A, Field JA, Sierra-Alvarez R. Cadmium telluride (CdTe) and cadmium selenide (CdSe) leaching behavior and surface chemistry in response to pH and O2. J Environ Manag 2015;154:78—85.

[66] Gui M, Papp JK, Colburn AS, Meeks ND, Weaver B, Wilf I, Bhattacharyya D. Engineered iron/iron oxide functionalized membranes for selenium and other toxic metal removal from power plant scrubber water. J Membr Sci 2015;488:79—91.

[67] Xie W, Li R, Xu Q. Enhanced photocatalytic activity of Se-doped TiO 2 under visible light irradiation. Sci Rep 2018;8:1—10.

[68] Bharti B, Kumar S, Lee H-N, Kumar R. Formation of oxygen vacancies and Ti3+ state in TiO2 thin film and enhanced optical properties by air plasma treatment. Sci Rep 2016;6:32355.

[69] Yu J, Gong C, Wu Z, Wu Y, Xiao W, Su Y, Sun L, Lin C. Efficient visible light-induced photoelectrocatalytic hydrogen production using CdS sensitized TiO 2 nanorods on TiO 2 nanotube arrays. J Mater Chem 2015;3:22218—26.

[70] Li W, li M, Xie S, Zhai T, Yu M, Liang C, Ouyang X, Lu X, Li H, Tong Y. Improving the photoelectrochemical and photocatalytic performance of CdO nanorods with CdS decoration. CrystEngComm 2013;15:4212—6.

[71] Li Y-S, Jiang F-L, Xiao Q, Li R, Li K, Zhang M-F, Zhang A-Q, Sun S-F, Liu Y. Enhanced photocatalytic activities of TiO2 nanocomposites doped with water-soluble mercapto-capped CdTe quantum dots. Appl Catal B Environ 2010;101:118—29.

[72] Huang K, Chen L, Deng J, Xiong J. Enhanced visible-light photocatalytic performance of nanosized anatase TiO 2 doped with CdS quantum dots for cancer-cell treatment. J Nanomater 2012;2012.

[73] Liqiang J, Yichun Q, Baiqi W, Shudan L, Baojiang J, Libin Y, Wei F, Honggang F, Jiazhong S. Review of photoluminescence performance of nano-sized semiconductor materials and its relationships with photocatalytic activity. Sol Energy Mater Sol Cell 2006;90:1773—87.

[74] Deshmane VG, Owen SL, Abrokwah RY, Kuila D. Mesoporous nanocrystalline TiO2 supported metal (Cu, Co, Ni, Pd, Zn, and Sn) catalysts: effect of metal-support interactions on steam reforming of methanol. J Mol Catal Chem 2015;408:202—13.

[75] Caglar A, Aktas N, Kivrak H. Tailoring cadmium composition on titanium dioxide to achieve enhanced photocatalytic glucose fuel cell anode performance. ACS Appl Energy Mater 2021;4:12298—309.

[76] Zhang N, Yang Z, Chen Z, Yunxiang L, Liao Y, Li Y, Gong M, Chen Y. Synthesis of sulfur-resistant TiO2-CeO2 composite and its catalytic performance in the oxidation of a soluble organic fraction from diesel exhaust. Catalysts 2018;8.

[77] Van Doorn J, Vuurman MA, Tromp P, Stufkens D, Moulijn J. Correlation between Raman spectroscopic data and the temperature-programmed oxidation reactivity of coals and carbons. Fuel Process Technol 1990;24:407–13.

[78] Barrie PJ. Analysis of temperature programmed desorption (TPD) data for the characterisation of catalysts containing a distribution of adsorption sites. Phys Chem Chem Phys 2008;10:1688–96.

[79] Zhou M, Liu P, Wang K, Xu J, Jiang J. Catalytic hydrogenation and one step hydrogenation-esterification to remove acetic acid for bio-oil upgrading: model reaction study. Catal Sci Technol 2016;6:7783–92.

[80] Choi H-J, Kim J-S, Kang M. Photodecomposition of concentrated ammonia over nanometer-sized TiŌ 2, V-TiŌ 2, and Pt/V-TiŌ 2 photocatalysts. Korean Chem. Soc 2007;28.

[81] Panahi PN, Delahay G. Activity of $\gamma$-Al $_{2}$ O $_{3}$-based Mn, Cu, and Co oxide nanocatalysts for selective catalytic reduction of nitric oxide with ammonia. Turk J Chem 2017;41:272–81.

[82] Hansu TA, Caglar A, Sahin O, Kivrak H. Hydrolysis and electrooxidation of sodium borohydride on novel CNT supported CoBi fuel cell catalyst. Mater Chem Phys 2020;239:122031.

[83] Caglar A, Cogenli MS, Yurtcan AB, Kivrak H. Effective carbon nanotube supported metal (M=Au, Ag, Co, Mn, Ni, V, Zn) core Pd shell bimetallic anode catalysts for formic acid fuel cells. Renew Energy 2020;150:78–90.

[84] Ulas B, Caglar A, Sahin O, Kivrak H. Composition dependent activity of PdAgNi alloy catalysts for formic acid electrooxidation. J Colloid Interface Sci 2018;532:47–57.

[85] Zhao S, Wang Y, Zhao Y, Sun X, Zhang H, Piao H-G, Zhang Y, Huang Y. The effect of magnetic field pretreatment on the corrosion behavior of carbon steel in static seawater. RSC Adv 2020;10:2060–6.

[86] Hamad AR, Calis H, Caglar A, Kivrak H, Kivrak A. Indole-based novel organic anode catalyst for glucose electrooxidation. Int J Energy Res 2022;46:1659–71.